Energy Storage Materials 67 (2024) 103302

Contents lists available at ScienceDirect

Energy Storage Materials

journal homepage: www.elsevier.com/locate/ensm

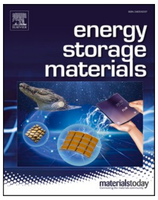

# Mg–Zn–Cl-integrated functional interface for enhancing the cycle life of Mg electrodes

Toshihiko Mandai [a,b,*], Umi Tanaka [b], Mariko Watanabe [b]

[a] Research Center for Energy and Environmental Materials, National Institute for Materials Science (NIMS), 1-1 Namiki, Tsukuba, Ibaraki 305-0044, Japan
[b] Center for Advanced Battery Collaboration, National Institute for Materials Science (NIMS), 1-1 Namiki, Tsukuba, Ibaraki 305-0044, Japan

ARTICLE INFO

*Keywords:*
Magnesium electrode
Interface
Surface modification
Short-circuit
Separator

ABSTRACT

The instability of the Mg-electrolyte interface in nonaqueous electrolytes hinders the realization of rechargeable Mg batteries (RMBs). Herein, we adopted surface engineering to address this issue by alleviating the passivation characteristics of reductive Mg electrodes. Among a series of artificial interfaces derived from different elements, the Mg–Zn–Cl-integrated artificial interface imparted outstanding Mg deposition–dissolution cycling performance upon combination with a halide-free weakly coordinated anion-based electrolyte. The artificial interface allowed Mg deposition–dissolution reactions beneath the interface, as evidenced by systematic scanning electron microscopy observations combined with electron backscatter diffraction analyses, and such interfacial characteristics suppressed the intrusion of Mg deposits into microporous separators, leading to remarkably stable cycling even under exceptionally high utilization conditions (>30 %). The amorphous nature induced by Cl integration improved interfacial stability during the successive morphological changes of Mg electrodes owing to electrochemical deposition–dissolution cycling. In addition, the artificial interface enabled the employment of a thin PTFE-based separator, which was unattainable using unmodified Mg. The developed techniques can pave the way for assessing the interfacial behavior under harsh, lean electrolyte conditions, which is an extremely important but unexplored research area of RMB chemistry.

## 1. Introduction

Mg and its alloys have attracted remarkable interest in the structural materials field as they possess the lowest densities among conventional metallic materials and exhibit efficient recyclability. The applications of Mg-based materials have been extended to vehicles, planes, and laptops, as well as active materials for energy storage devices. Rechargeable Mg batteries (RMBs), where Mg serves as an active negative electrode material, offer high abundance, cost-effectiveness, high chemical stability, sufficiently low standard electrode potential, and high specific/volumetric capacities for the realization of next-generation batteries [1,2]. However, despite the potential of RMBs and recent dramatic advancement in the development of individual battery components [3–10], several challenges impede the realization of RMBs.

One of the significant obstacles to RMB realization is the instability of the Mg-electrolyte interface. Mg cells often suffer from cell failure despite the morphological (spherical, nevertheless nondendritic) aspects of Mg deposits [11,12]. Cui and co-workers reported a current-density-driven dissolution behavior of the Mg metal [13]. The self-accelerating pit growth mechanism of neither kinetically controlled nor homogenizing regions at certain current densities can lead to the failure of Mg electrodes. In addition, the systematic morphological and metallurgical analyses revealed inhomogeneous passivation-driven peculiar three-dimensional (3D) deposition behavior [6]. The passivation characteristics of Mg electrodes, caused by the side reactions of Mg with electrolyte components and atmospheric impurities [10,14–17], can even hinder effective $Mg^{2+}$ conduction at the Mg-electrolyte interface, reducing electrochemical performance. To overcome these interfacial issues, considerable research efforts have been devoted to stabilizing the interface using bulk and interfacial approaches.

Establishing an artificial interface that possesses good $Mg^{2+}$ conduction characteristics while simultaneously suppressing passivation due to electrolytes can be a straightforward approach to effective interface control. Several interfacial engineering techniques have been reported for Mg electrodes, such as coating the nonpassivating $Mg^{2+}$ conductive layer [18,19], chemical pretreatment with certain elements

---

[*] Corresponding author at: Research Center for Energy and Environmental Materials, National Institute for Materials Science (NIMS), 1-1 Namiki, Tsukuba, Ibaraki 305-0044, Japan.

*E-mail address:* MANDAI.Toshihiko@nims.go.jp (T. Mandai).

https://doi.org/10.1016/j.ensm.2024.103302
Received 14 November 2023; Received in revised form 14 January 2024; Accepted 25 February 2024

[20–25], and the in situ construction of the protective layer using functional additives [26–30]. Interfacial engineering can modulate the highly reductive nature of the Mg metal and provide favorable Mg deposition–dissolution characteristics. Coupling these pretreatment approaches with highly reactive organohaloaluminate-based electrolytes results in excellent cycling properties even at high current densities [20,31]. Functional additives mostly involve halide species (mainly chloride). The addition of halides in electrolytes results in electrochemically active Mg–Cl-bridged complex formation in these organohaloaluminate-based electrolytes [32,33] and simultaneously regulates interfacial kinetics upon functional layer formation. However, the poor compatibility of halide-containing electrolytes against non-noble metals and positive-electrode materials hinders their application to RMBs [34]. Moreover, the combination of highly thick microporous glass fiber (GF) separators, e.g., GF/D ($t$ = 0.680 mm) and thick Mg metal, e.g., $t$ = 0.100 mm, as often employed in the preceding works, makes it difficult to reveal the role of interfacial engineering under practical conditions. Indeed, the cycling characteristics of metal electrodes strongly depend on the utilization ratio [35–37]. Thus, the cycling performance must be tested under practical conditions using relatively thin separators to realize high-energy-density batteries [6,38].

In this study, we demonstrate a surface engineering approach combined with the use of halide-free electrolytes to achieve a robust interface, which enables the construction of high-energy-density RMBs. The recently developed weakly coordinated anion (WCA)-based electrolytes exhibit remarkable compatibility with Mg negative and high-voltage positive electrodes [8,39,40]. Among them, Mg[Al(HFIP)$_4$]$_2$/G2 (HFIP: hexafluoro-iso-propoxyl group) electrolyte exhibits excellent Mg deposition–dissolution efficiencies and superior compatibility with various positive-electrode materials, including $Mo_6S_8$, polyanthraquinone, and elemental sulfur [41,42]. By combining a $ZnCl_2$-derived artificial interface with the proposed electrolyte, the Mg deposition–dissolution characteristics are enhanced even with a relatively thin GF separator at a high utilization ratio of >30 % for the ultrathin Mg foil electrode. In addition, the obtained Mg-electrolyte interface allows stable cycling in the presence of a thin PTFE separator, whereas the cells employing nontreated Mg fail immediately. The systematic microscopic and structural analyses reveal the formation of a $Mg^{2+}$-conductive amorphous Mg–Zn–Cl-integrated functional interface, which is bound to the Mg metal surface strongly and allows Mg deposition–dissolution beneath the interface.

## 2. Experimental

### 2.1. Materials

Mg[Al(HFIP)$_4$]$_2$ and Zn[B(HFIP)$_4$]$_2$ were synthesized according to the established procedures [41,43]. Diglyme (G2), monoglyme (G1), and tetrahydrofuran (THF) designated for electrochemical measurements were purchased from Kanto Chemical CO., Inc., and used without further purification. A THF solution of $C_2H_5MgCl$ (ca. 2 mol dm$^{-3}$; as a representative Grignard reagent) was purchased from Tokyo Chemical Industry CO., Ltd. Triflate and chloride salts of Bi, Sn, Zn, and Mg were obtained in the solid form, except $ZnCl_2$, and used for the surface engineering of Mg and as electrolyte additives, after drying under vacuum heating at 80 °C for 3 days. $ZnCl_2$ was purchased as an anhydrous THF solution (ca. 0.5 mol dm$^{-3}$). $Cu_2Mo_6S_8$ was purchased from Kojundo Chemical Laboratory Co. Ltd. and oxidized to obtain Cu-free $Mo_6S_8$ powder following a standard oxidation protocol [44].

### 2.2. Preparation of electrolytes

The base electrolyte solution of 0.3 mol dm$^{-3}$ Mg[Al(HFIP)$_4$]$_2$/G2 was prepared by dissolving predetermined amounts of the salt in G2. This solution was then vigorously stirred overnight at 30 °C within an Ar-filled glovebox ($O_2$, $H_2O$ <1 ppm, UNICO). For obtaining the Zn- or Cl-integrated solutions, a predetermined amount of Zn[B(HFIP)$_4$]$_2$, $ZnCl_2$, or $MgCl_2$ was added to the base electrolyte. The concentration of the Mg[Al(HFIP)$_4$]$_2$ salt in these solutions was fixed at 0.3 mol dm$^{-3}$, unless specified otherwise. The water content of each electrolyte was measured to be <30 ppm, as determined using the Karl Fischer titration.

### 2.3. Preparation of an artificial interface on Mg electrodes

An artificial interface was formed on Mg electrodes to improve cyclability. Mechanically polished Mg disks (99.94 %, $\varphi$ = 16 mm, $t$ = 0.04 mm) were soaked in various pretreatment solutions, predominantly in 0.1 mol dm$^{-3}$ ethereal solutions, for 1 and 5 h at a temperature of 30 °C. The treated Mg disks were then washed with anhydrous G1 to remove any residual pretreatment solutions followed by vacuum drying to obtain the working electrodes for galvanostatic Mg dissolution–deposition measurements and battery tests.

### 2.4. Electrochemistry

Galvanostatic measurements were conducted for asymmetric and symmetric two-electrode cells. Asymmetric cells were fabricated using Cu foil and the treated Mg metal, whereas two treated Mg metals were used for the symmetric cell assembly. The cells using untreated Mg metals were also fabricated as a reference. A series of GF filters with different microstructures and thicknesses, purchased from ADVANTEC and Whatman, and conventional polyolefin-based microporous membranes were used as separators. The physical parameters of the GF filters are summarized in Table S1. To observe the step-by-step morphological evolution of the cycled Mg via SEM analyses, a PTFE ring spacer was utilized in the cell assemblies to prevent the peeling off of the interface from electrode samples during disassembly. All cell assemblies were performed within an Ar-filled glovebox. All galvanostatic cycling measurements were conducted using an automatic charge–discharge instrument (HJ0610SD8C, Hokuto-Denko Co., Ltd.) at a current density of 0.5 and 1 mA cm$^{-2}$ for predetermined periods. For cyclic voltammetry, typical three-electrode-type cells were used to examine the electrochemical Mg deposition–dissolution behavior of the Zn- and Cl-integrated electrolytes. A platinum disk ($\varphi$ = 3 mm, BAS), Mg ribbon (98.5 % purity, FUJIFILM Wako Chemicals), and $Ag^+$/Ag electrodes served as the working, counter, and reference electrodes, respectively. The electrode potential of the reference $Ag^+$/Ag was determined to be +2.49 V vs. $Mg^{2+}$/Mg, as reported elsewhere [11,41]. Each test was repeated at least three times separately to ensure experimental reproducibility. For the charge–discharge cycling tests, composite positive electrodes were fabricated by mixing $Mo_6S_8$ powder, carbon nanotube/fluoropolymer dispersion (NEOFLON VTD-475N; Daikin Industries, Ltd.), acetylene black (AB), and polyvinylidene difluoride (PVdF) in a weight ratio of 92:0.5:3.5:4. This mixture was homogenized in *N*-methylpyrrolidone to obtain slurry, which was then spread onto an Al foil current collector and dried at 80 °C for several days. To enhance electrical conductivity, the resultant composite sheet was compressed. The average loading of $Mo_6S_8$ was fixed at ca. 4 mg cm$^{-2}$. Two-electrode cells comprising the $Mo_6S_8$ composite electrode ($\varphi$ = 16 mm), Mg negative electrode (φ = 16 mm), glass fiber separator (GF/A, $t$ = 0.260 mm, φ = 17 mm), and the base electrolyte (150 μL) were assembled in a glovebox. The cycling test was conducted within a voltage range of 0.3–1.8 V at 30 °C with a current density of 12.2 mA g$^{-1}$ based on the $Mo_6S_8$ mass using an automatic charge–discharge instrument.

### 2.5. Chemical, structural, and morphological analysis

The surface chemical/structural nature and morphological aspects of the treated Mg samples were characterized using X-ray photoelectron spectroscopy (XPS; VersaProbe II, ULVAC-PHI), X-ray diffraction (XRD; SmartLab, Rigaku), and scanning and transmission electron microscopy (SEM, JSM-7800F, JEOL; STEM, EM-ARM200F, JEOL) combined with energy-dispersive X-ray spectrometry (EDX) and electron energy loss spectroscopy (EELS). XPS measurements were conducted with an Al Kα X-ray source under a base pressure of less than 6.7 × $10^{-8}$ Pa. The binding energy of the obtained spectra was calibrated using the C 1 s peak of *sp*2-hybridized carbon at 284.5 eV as a reference. Grazing incidence (GI)–XRD profiles were acquired using Cu Kα radiation ($\lambda$ = 1.54078 Å) to examine the surface nature of the treated and cycled Mg electrodes. The surface and cross-sectional morphologies of the treated Mg and separators were observed using SEM and TEM, and the distribution of elements was subsequently characterized using EDX and EELS. The retrieved electrode and separator samples were processed using a focused ion beam to obtain a smooth cross-sectional view. To avoid any exposure to the air, the processed samples were placed in a designated airtight chamber and transferred for each analysis or measurement.

The solubility of Zn-based artificial interfaces was investigated by inductively coupled plasma mass spectrometry (ICP-MS). The electrolyte solutions were extracted using G1 from the cycled asymmetric [Zn-treated Mg || Cu] cells, followed by dilution with deionized water, and then subjected to the ICP-MS instrument. Two individual cells were prepared for each experiment, and the average of the concentrations of Zn leached out from the artificial interfaces was determined.

## 3. Results and discussion

### 3.1. Revisiting the short-circuiting of Mg cells

Prior to examining the role of interfacial engineering, it is useful to review the interfacial behavior and consequent short-circuit phenomena of Mg cells. The electrochemical cells with Mg electrodes often suffer from the shortage phenomena upon repeated electrochemical cycling despite the characteristic morphological aspects of Mg deposits in nonaqueous electrolytes. Recent studies demonstrated typical fractal, dendritic growth of Mg under a specific diffusion-limited (high-current-density) condition [45,46]. However, as shown in Fig. S1, undesired short-circuit phenomena took place immediately after applying sufficiently low current density for typical two-electrode assemblies using organic microporous separators ($t$ = 20 μm). The SEM images and corresponding EDX profiles of the cross-sectional view of the representative polyolefin-based separator after a single deposition process at 0.5 mA $cm^{-2}$ for 0.5 h (0.25 mAh $cm^{-2}$, which corresponds to only 0.5 μm-thick Mg deposition) indicate severe intrusion of deposits into the micropore of the separator (Fig. S2). The thicker polyolefin-based separators, i.e., ≥100 μm thickness, do not allow stable galvanostatic cycling, whereas thick PTFE-based separators showed relatively stable cycling profiles (Fig. S3). These results strongly imply the exceptionally poor compatibility of polyolefin-based separators against Mg.

Using inorganic thick separators, *i.e.*, GF separators, these

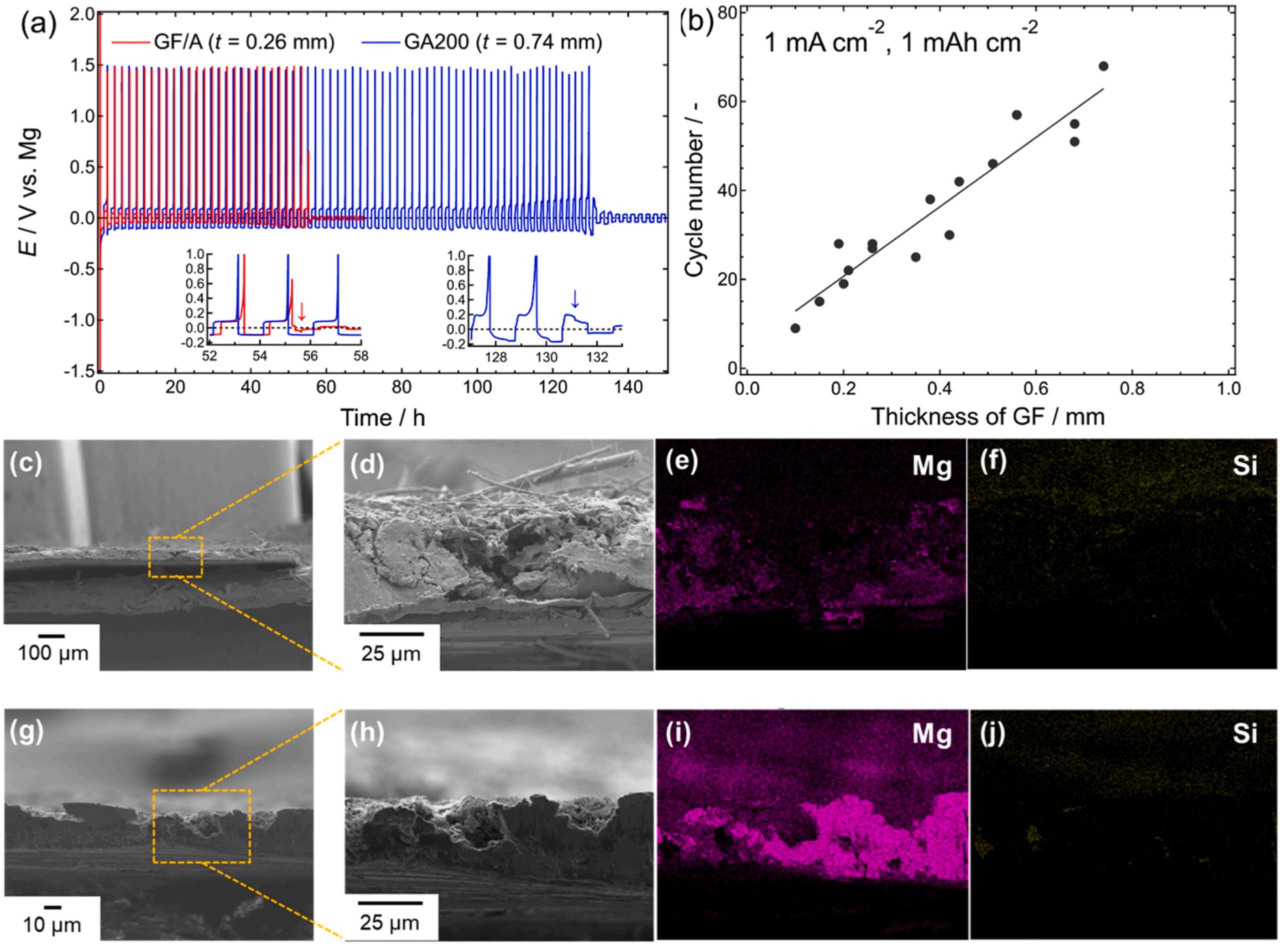

**Fig. 1.** (a) Galvanostatic Mg deposition–dissolution cycling profiles of [Mg || Cu] cells using representative GF separators. The measurements were conducted using 0.3 mol $dm^{-3}$ $Mg[Al(HFIP)_4]_2$/G2 electrolyte at a geometrical current density of 1 mA $cm^{-2}$ for 1 h. (b) Relationship between the thickness of GF separators and cycle life of [Mg || Cu] cells. The result of the linear fitting analysis is included as a straight line. (c), (d), (g), and (h) Cross-sectional SEM images and (e), (f), (i), and (j) the corresponding Mg and Si EDX profiles of the cycled (c–f) GF/A separator and (g–j) Mg electrode. The thickness of the retrieved separator considerably decreased from the original value ($t$ = 0.260 mm) owing to the compression during cell fabrication. Arrows in insets of (a) indicate the timing where short circuits occur.

catastrophic events can be mitigated but cannot be addressed completely. Fig. 1 summarizes the cycle lives of the asymmetric [Mg || Cu] cells against the thickness of the employed GF separators. In this study, the cycle life is defined as the cycle number at which symmetric square waves are observed for the galvanostatic cycling of asymmetric cells. An intriguing relationship between the thickness and cycle life is observed (Fig. 1a and b), whereas the cycle life is independent of the other GF parameters, such as the nominal filtration rating and bulk density (Table S1, Fig. S4). These results indicate the peculiar 3D growth of Mg upon repeated cycling. The thickness-dependent capable cumulative capacities of Mg electrodes were reported by Pint et al. [12]. They attributed the 3D hemispherical growth of Mg deposits in conventional ethereal solutions of $Mg[N(CF_3SO_2)_2]$ to unexpected cell failure. The pit growth mechanisms of Mg electrodes during dissolution processes also accelerate uneven utilization and enhance highly localized 3D morphological evolution [13]. Although the localization of 3D morphological evolution can be modulated upon increasing applied current densities over the homogenizing region, i.e., >10 mA $cm^{-2}$, the intrinsic uneven distribution of the active sites of bulk Mg metal leads to uneven utilization and nonuniform current density distribution for the subsequent cycles [6]. Indeed, a relatively poor correlation between the applied geometrical current densities and cycle lives was observed using GF separators with different thicknesses (Fig. S5).

The cross-sectional views of the cycled separators exhibit cell failure. Fig. 1c and d display the SEM images of the GF/A separator retrieved from the cycled cells (the corresponding profile is shown in Fig. 1a). The separator is partly filled with deposited Mg; hence, it no longer functions as an electron-insulating layer. The deposited Mg left in the separator comes from the Mg counter electrode. Indeed, the morphology of the Mg electrode drastically changed upon galvanostatic cycling, as shown in Fig. 1g and h. The uneven active-site distribution and peculiar electrochemical deposition behavior of Mg metals may cause such destructive morphological evolution.

### 3.2. Electrochemical characteristics of surface-modified Mg

Simple galvanic replacement reactions were adopted in this study to enhance the cycle lives of Mg electrodes upon interfacial modification. Owing to the reductive nature of Mg, spontaneous reactions take place upon immersing Mg metals in certain solutions containing ions of less reductive metals, such as Bi, In, Ga, Sn, and Zn. According to previous works on the Mg surface modification using different elements [22,24,27,47], Bi, Sn, and Zn were selected, and their effects on the cycling performance were investigated. To highlight the efficacy of the surface modification on the performance, a relatively thin GF separator, GF/A ($t$ = 0.260 mm), was employed unless otherwise specified.

The galvanostatic Mg deposition/dissolution profiles of asymmetric [Mg || Cu] cells using modified Mg electrodes are summarized in Fig. 2. Surface-modified Mg electrodes were prepared by immersing mechanically polished Mg disks ($\Phi = 16$ mm) in 0.1 mol $dm^{-3}$ ethereal solutions of Bi, Sn, and Zn chloride for 5 h, followed by washing with an anhydrous G1 solvent several times, and then dried under vacuum. The formation of each element-based interlayer was confirmed using SEM and EDX (Fig. S6). As shown in Fig. 2, the modified element-dependent cycling performance was observed. An exceptionally significant improvement was achieved for the cells with the $ZnCl_2$-modified Mg, whereas the magnitude of the improvement was modest for the $BiCl_3$-modified Mg. In the case of the cells with the $SnCl_2$-modified Mg, an inferior performance was observed. Surface modification using $SnCl_2$/G1 was shown to be effective in improving interfacial ion transport characteristics upon artificial alloy layer formation [53]. The opposite results obtained here may be due to the difference in the composition of the interlayer. For the reported procedure, the modified Mg was prepared by dropping the $SnCl_2$/G1 solution, followed by drying. Thus, Sn and Cl species remained on the surface. In contrast, our modified Mg electrode surface was washed with G1 to remove remaining chemicals, such as unreacted $SnCl_2$ and $MgCl_2$ by-products. Indeed, the interface contained a strong contribution of Cl species for the reported electrodes, as evidenced by EDX and XPS analyses, whereas the contribution of Cl

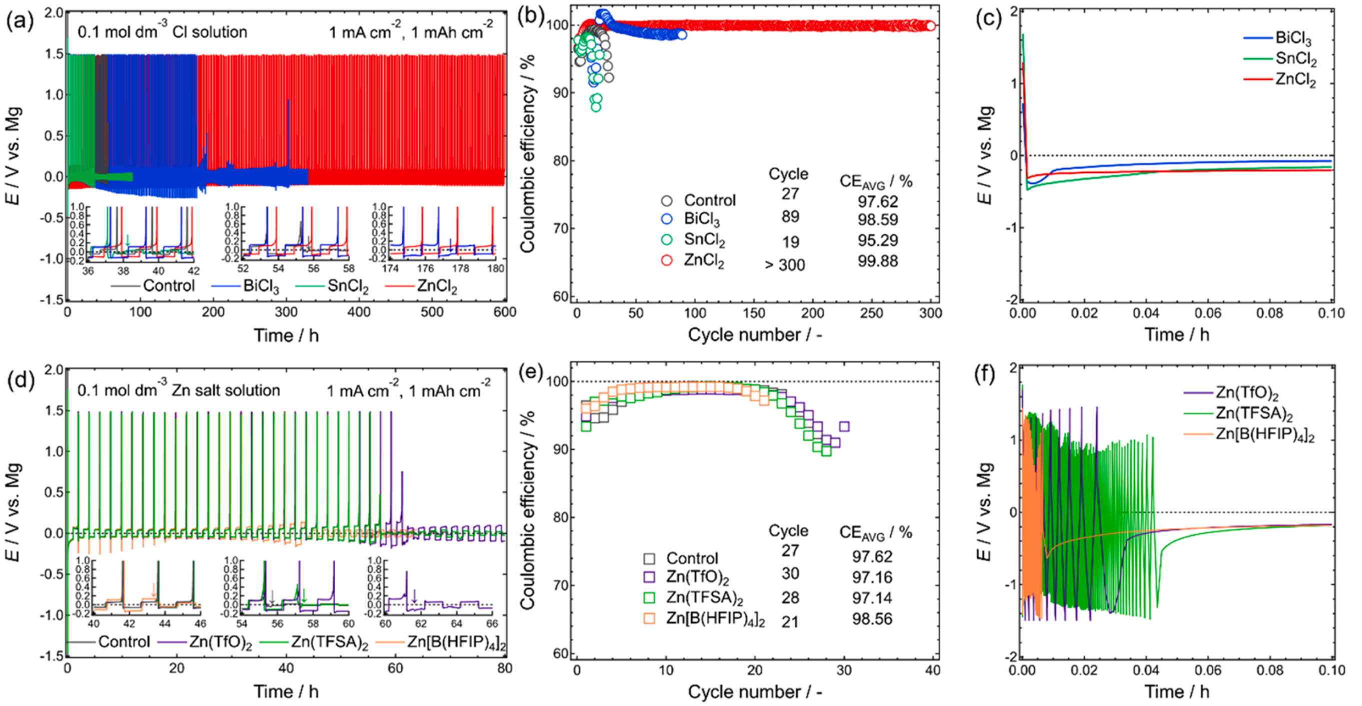

**Fig. 2.** (a, d) Galvanostatic cycling profiles, (b, e) corresponding Coulombic efficiencies, and (c, f) magnified initial deposition profiles of asymmetric [modified Mg || Cu] cells at a current density of 1 mA $cm^{-2}$. Mg electrodes were modified using a series of 0.1 mol $dm^{-3}$ (a–c) Cl and (d–f) Zn salt solutions. A typical GF film, GF/A ($t$ = 0.260 mm), was employed as a separator. The results obtained using untreated Mg electrodes are included as a reference. Arrows in insets of (a) and (d) indicate the timing when short circuits occur.

components was considerably weak in this study compared to those of Bi, Sn, and Zn, suggesting the effective removal of Cl species from the modified interface, except for the $ZnCl_2$-treated Mg (Fig. S7). As the remaining Cl affects electrochemical properties, the absence of such active species resulted in relatively inferior performance for the $SnCl_2$- and $BiCl_3$-modified Mg electrodes. Conversely, the integration of Cl species resulted in the effective stabilization of electrochemical Mg dissolution–deposition behavior. Undesired penetration of deposits into the porous GF separator was suppressed upon utilizing the $ZnCl_2$-modified Mg electrodes even after substantially extended galvanostatic cycling (Fig. S8). The inferior cycling performances of the cells employing the Mg electrodes modified with Cl-free Zn-based compounds further support the effectiveness of the integration of Cl species to improve the electrochemical activity of Mg electrodes. Neither positive nor negative effects were found for the Mg electrodes modified with $Zn(TfO)_2$, $Zn(TFSA)_2$, and $Zn[B(HFIP)_4]_2$ solutions (Fig. 2d); nevertheless, certain Zn species were involved in the modified interface (Fig. S9).

In addition to the cycle life, interfacial modification considerably affects the initial dissolution overpotential. For the unmodified Mg electrode, repeated alternating positive and negative polarization processes, so-called activation processes, are required to initiate the electrochemical dissolution–deposition activity owing to the highly insulating nature of the native surface film (Fig. S10). Such activation processes disappeared for the cells employing the Cl-modified Mg electrodes (Fig. 2c and f), indicative of the removal of the native insulating film upon chemical treatment with Cl-containing solutions.

Reducing the Mg pretreatment time without compromising the remarkable characteristics of modified Mg electrodes is vital from an industrial and manufacturing perspective. Unfortunately, attempts to reduce the immersion time from 5 h to 1 h were unsuccessful, resulting in an interface with inferior performance (Fig. S11). The limited activity of Zn(II) species is due to its low dissociativity (~$10^{-6}$ S $cm^{-1}$ for 0.1 mol $dm^{-3}$ $ZnCl_2$/G1 at 30 °C) and resulting slow kinetics of the replacement reaction contributed to this outcome. The surface of Mg electrodes immersed for 1 h was covered inhomogeneously with reaction products (Fig. S11).

The electrochemical Mg dissolution–deposition characteristics of the $ZnCl_2$-modified Mg electrodes were further examined using various experimental conditions. The immersion time for modification by $ZnCl_2$ was set to 5 h. The $ZnCl_2$-modified electrodes allowed remarkably stable galvanostatic cycling over 1500 h (>750 cycles) at a current density of 1 mA $cm^{-2}$, whereas a short circuit took place for the unmodified counterpart (Fig. 3a). In addition, the $ZnCl_2$-modified electrodes enabled cycling for a larger areal capacity of 5 mAh $cm^{-2}$, which corresponds to approximately 30 % utilization ratio against the 40-μm-thick Mg metal. To achieve a Mg battery with an energy density of 300 Wh $kg^{-1}$, Mg electrodes with a thickness of less than 40 μm must be coupled with cathodes having an areal capacity of at least 4 mAh $cm^{-2}$ based on the energy density calculator [38]. At such a large areal capacity, the unmodified electrode did not support galvanostatic cycling as a short circuit took place at an initial step owing to the severe intrusion of deposits into the separator and consequent percolation driven by uneven utilization. In stark contrast, the $ZnCl_2$-modified electrode allowed stable galvanostatic cycling over 70 cycles with extremely high Coulombic efficiencies of >99.9 % at a sufficiently high utilization ratio (Fig. 3b).

Moreover, the $ZnCl_2$ modification on Mg electrodes was effective in improving the rate capability. For the unmodified Mg electrodes, the overpotential for Mg dissolution and deposition gradually increased with increasing current density; however, the overpotential suddenly decreased to ca. 20 mV at a current density of 2 mA $cm^{-2}$, which indicates a short circuit as the symmetric square wave can be seen in their subsequent cycling profiles (Fig. 3c). By contrast, for the $ZnCl_2$-modified

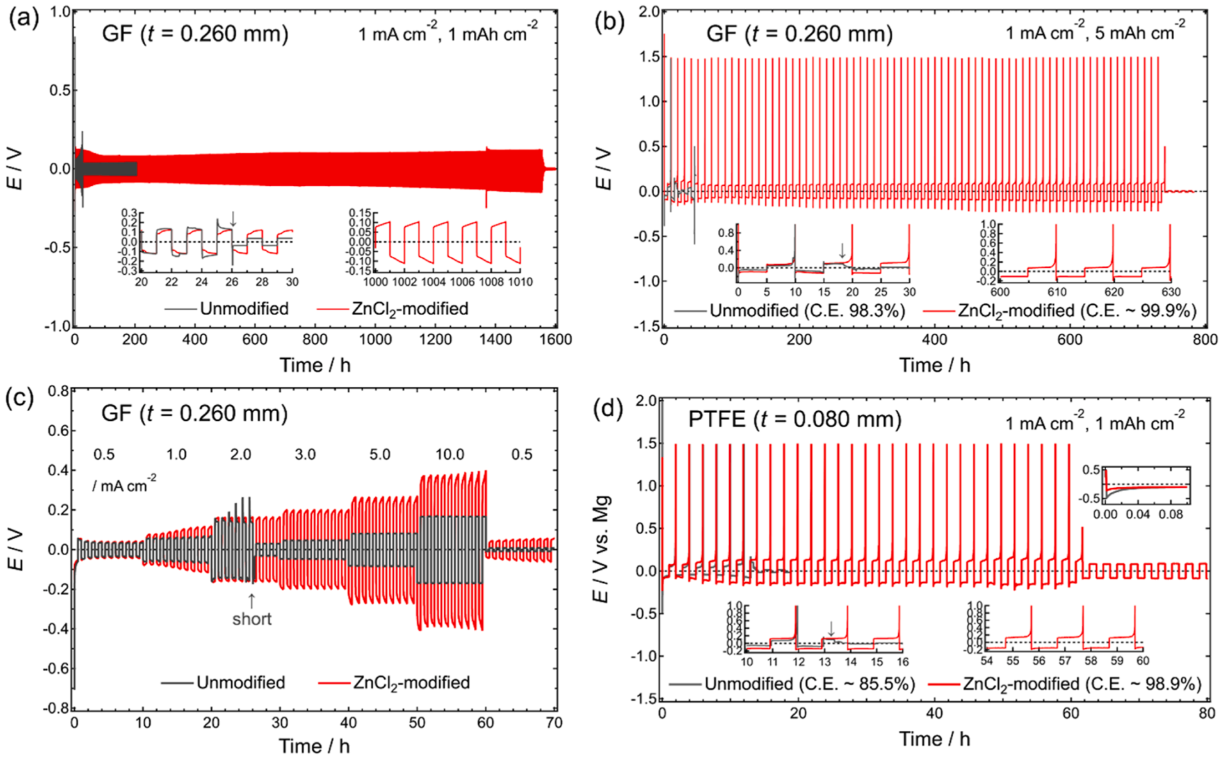

**Fig. 3.** (a) Long-term galvanostatic cycling profiles of symmetric cells with a GF/A separator at a current density of 1 mA $cm^{-2}$ for 1 h. (b) Galvanostatic cycling profiles of asymmetric [Mg || Cu] cells at a current density of 1 mA $cm^{-2}$ for 5 h (5 mAh $cm^{-2}$), corresponding to the 32.5 % utilization ratio of a Mg foil with a thickness of 40 μm. (c) Polarization curves of symmetric cells at different current densities. (d) Galvanostatic cycling profiles of asymmetric cells with a typical PTFE membrane filter ($t$ = 0.080 mm) at a current density of 1 mA $cm^{-2}$ for 1 h. Inset: magnified profile at an initial period. Zn-modified Mg electrodes exhibit much favorable electrochemical performance, regardless of the experimental conditions. Arrows in (c) and insets of (a), (b), and (d) indicate the timing when the short circuits occur.

electrodes, the typical galvanostatic cycling profiles of symmetrical cells were obtained even at a current density of 10 mA cm$^{-2}$, indicating that Mg deposition–dissolution processes are not limited by mass transport but by the charge transfer at the interface, and the $ZnCl_2$-modified interface effectively promotes interfacial charge transport kinetics. The overpotential at an applied current density of 0.5 mA cm$^{-2}$ after 60 cycles of galvanostatic cycling was identical to that at the same current density for the initial condition, indicating the sufficiently stable interface for the $ZnCl_2$-modified Mg electrodes.

Furthermore, the $ZnCl_2$-modified interface was compatible with the PTFE-based organic membrane filter. The PTFE separator was substantially thinner than our standard GF separator (0.080 mm for the former and 0.260 mm for the latter). Nevertheless, the PTFE separator allowed stable galvanostatic cycling over 30 cycles at an areal capacity of 1 mAh cm$^{-2}$ upon combination with the $ZnCl_2$-modified Mg electrodes (Fig. 3d). Note that, polyolefin-based separators continued to not support any Mg deposition–dissolution cycling even with $ZnCl_2$-modified Mg, suggesting fundamentally poor compatibility of polyolefin-based separators for Mg deposition (Fig. S12). Although the areal capacity and cycle life of our systems seem insufficient for practical use, the present $ZnCl_2$ modification has considerable potential to enhance the energy density of Mg batteries upon replacing GF separators with thinner and lighter organic membrane-based separators.

The advantages of $ZnCl_2$-modified Mg electrodes were also observed in battery cycling measurements. Fig. 4 displays the galvanostatic discharge–charge cycling profiles of the [Mg || $Mo_6S_8$] cells based on the $ZnCl_2$-modified and unmodified Mg electrodes. The initial discharge capacities were comparable irrespective of whether the $ZnCl_2$-modified Mg was employed or not; however, the capacity retention upon repeated cycling and polarization for discharge and charge considerably improved upon $ZnCl_2$ modification. For the cell constructed with unmodified Mg, the deliverable capacities diminished rapidly upon cycling owing to increased polarization. At the 10th cycle, the polarization between the discharge and charge reached ca. 0.8 V, and the plateau voltage for discharge changed completely from that of the original value, from 1.0 V to 0.5 V, implying a change in the reaction mechanism corresponding to discharge processes. In the case of the $ZnCl_2$-modified Mg, the deliverable capacity stabilized at approximately 60 mAh g$^{-1}$ for the initial 10 cycles and gradually diminished upon cycling, whereas the magnitude was substantially small (only 0.025 mAh g$^{-1}$ after a single cycle). The polarization for discharge–charge remained largely unchanged, with the observed voltage plateaus overlapping across cycles, implying remarkably stable electrochemical reaction at the $Mo_6S_8$ cathode and electrode potential at the Mg electrodes owing to the interfacial modification of the Mg electrodes with $ZnCl_2$. Note that the self-discharging phenomena were observed in cells with $ZnCl_2$-modified Mg. Furthermore, similar results have been reported in literature irrespective of whether the Mg was modified [48–51]. Although the detailed mechanism underlying the self-discharging of $Mo_6S_8$ remained unclear, the crossover of interfacial components to $Mo_6S_8$ electrodes and consequent stimulation of spontaneous Mg insertion into the $Mo_6S_8$ structure account for these observations [52].

The comparative experiments on electrolytes further confirmed the advantageous characteristics of $ZnCl_2$-modified Mg electrodes prepared using galvanic replacement. Electrolytes containing $Zn^{2+}$ and $Cl^-$ additives individually did not show improved electrochemical performances. The sole integration of $Zn^{2+}$ species to electrolyte solutions and interface had minor impacts on electrochemical Mg deposition–dissolution activities (Figs. 2 and S13). Meanwhile, the effect of the addition of solely Cl species on the electrochemical performances was also negligible as no significant improvement was observed in our experiments with $MgCl_2$ additive (Fig. S14) as well as a preceding work [42]. In addition to the integration of Zn and Cl species individually, the direct integration of $ZnCl_2$ into the electrolyte solutions minimally impacted the electrochemical performances (Fig. S15). Although the identification of the detailed composition and formation mechanism of the interface from $ZnCl_2$-integrated base electrolytes is outside the scope of this study, this nontrivial result strongly suggested the coexistence of base electrolyte components, $Mg^{2+}$ and $[Al(HFIP)_4]^-$, preventing the formation of a favorable interface derived from $ZnCl_2$.

### 3.2.1. *Mechanistic understanding of improved cycle life upon surface modification with $ZnCl_2$*

To understand the positive effects of $ZnCl_2$ modification on enhancing the interfacial and electrochemical properties of Mg electrodes, the physical structure and chemical composition of the interface were investigated using a combination of microscopic analytical techniques. Figs. 5 and 6 display microscopic analytical data for the $ZnCl_2$-modified and $Zn(TfO)_2$-modified Mg electrodes, respectively, obtained using SEM and STEM measurements. The $ZnCl_2$-modified Mg surface exhibited a coral-like morphology due to the presence of reaction products (Fig. 5a and b). The subsequent STEM analysis revealed the formation of a complex hierarchical structure on the Mg substrate owing to $ZnCl_2$-modification. While the coral-like structure could be assigned to Zn metal with a small fraction of $Mg_xZn_y$ alloy (Fig. 5f), a highly amorphous MgO layer (presumably containing $MgCl_2$ as well) was interposed between the substrate and Zn. Formation of a similar interface was reported for the amorphous MgO-wrapped Zn-skeleton [24]. The outermost layer of the substrate, i.e., the layer beneath the amorphous MgO, was likely a $Mg_xZn_y$ alloy. The line profile of EELS spectra also supported the formation of this intricate architecture (Fig. 5k), showing discernible profiles of $Mg_xZn_y$ alloy when scanned from the bottom (Mg metal substrate) to surface. Furthermore, the abrupt emergence of the MgO layer and then a gradual shift from MgO with $Mg_xZn_y$ alloy to Zn metal were observed in the EELs analyses. Notably, the EELS spectra of $Mg_xZn_y$ were speculative due to the lack of a reference, while those of Mg, Zn, MgO, and ZnO were identified using the corresponding references (Fig. S16) [53,54].

Conversely, the $Zn(TfO)_2$-modified Mg interface appeared simpler, as shown in Fig. 6. Needle-like bulk crystalline Zn metal was sporadically deposited on the surface of the Mg substrate, with a thin MgO layer forming the interface between Zn and Mg. Unlike the $ZnCl_2$-modified Mg, no evidence of Mg–Zn alloy formation was found for the $Zn(TfO)_2$-modified sample. EDX and EELS line profiles delineated a distinct

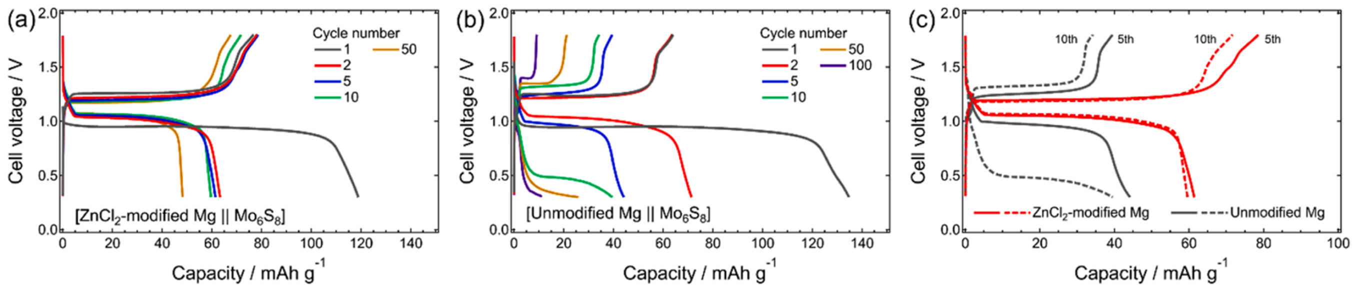

**Fig. 4.** Discharge–charge profiles of [Mg || $Mo_6S_8$] cells using (a) $ZnCl_2$-modified and (b) unmodified Mg electrodes at a current density of 10 mA g$^{-1}$. (c) Comparisons of the polarization behavior of the two electrodes at the 5th and 10th cycles.

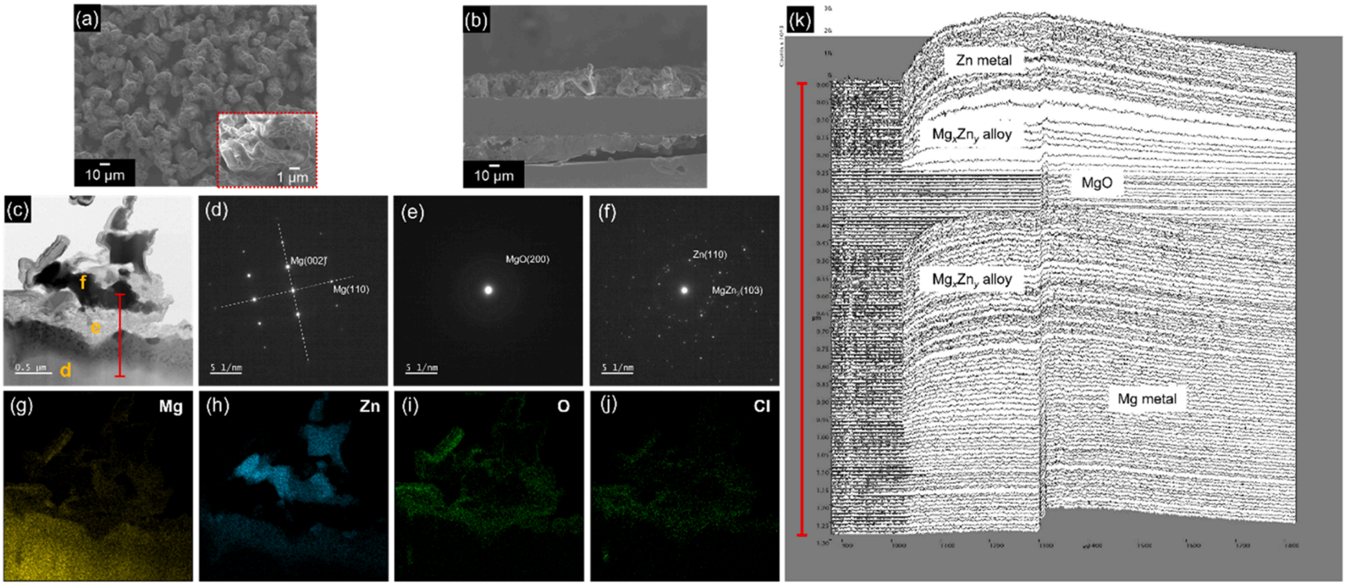

**Fig. 5.** Microscopic analytical data of $ZnCl_2$-modified Mg. SEM images of the (a) surface and (b) cross-section. (c) Bright-field STEM image and corresponding (d–f) position-resolved electron diffraction patterns for specific positions specified in (c), and (g–j) EDX profiles. (k) Line profile of EELS spectra corresponding to Mg–*L* and Zn–*L* edges. Red line shown in (c) indicates the line scan area.

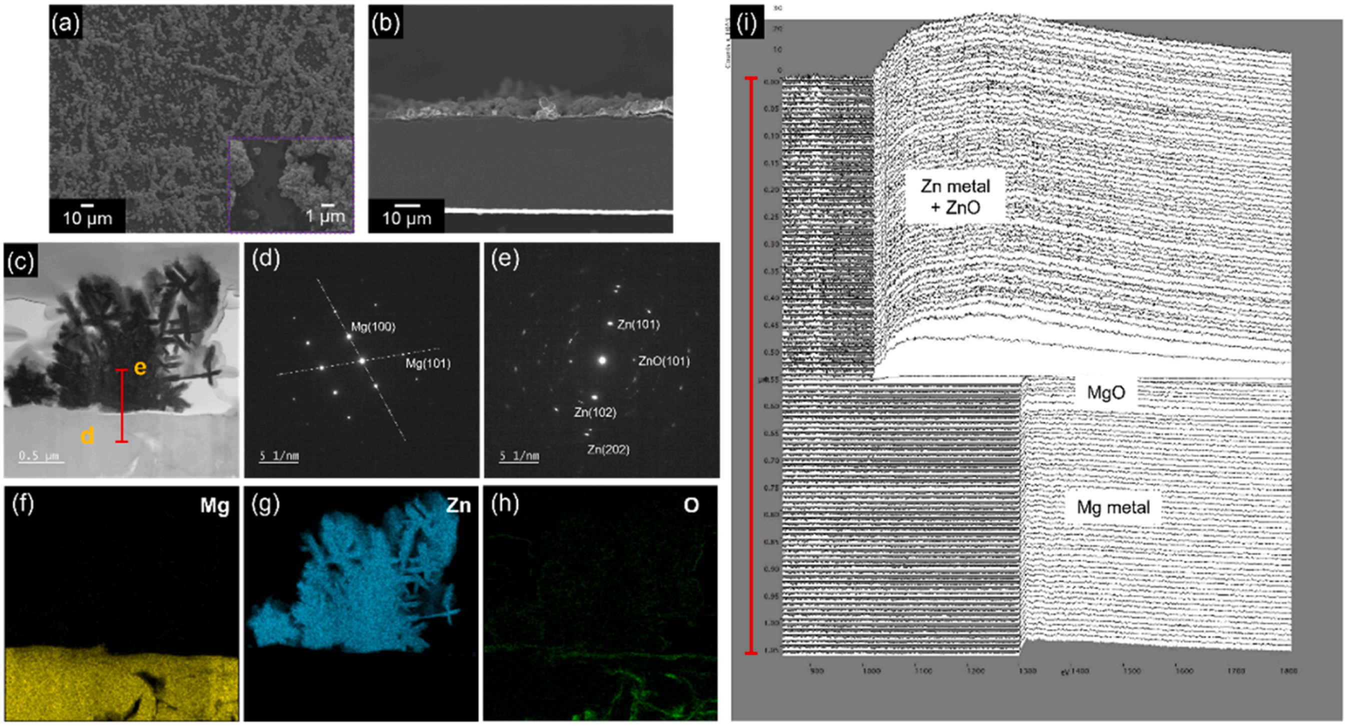

**Fig. 6.** Microscopic analytical data of $Zn(TfO)_2$-modified Mg. SEM images of the (a) surface and (b) cross-section. (c) Bright-field STEM image and corresponding (d, e) position-resolved electron diffraction patterns of specific positions specified in (c), and (f–h) EDX profiles. (i) Line profile of EELS spectra. Red line shown in (c) indicates the line scan area.

boundary between Zn deposits and Mg substrate as there were no signals indicative of intermetallic compounds at the interface. The differing mechanisms for the replacement reaction of Mg with $ZnCl_2$ and $Zn(TfO)_2$ solutions might stem from the solubility of reaction products—$MgCl_2$ was hardly soluble in ethereal solvents while, $Mg(TfO)_2$ could be dissolved to some extent in same solvents over a relatively broad concentration range [55,56]. The strong Lewis basicity of $Cl^-$ might contribute to its binding with neighboring $Mg^{2+}$ and $Zn^{2+}$ at reaction sites, potentially leading to the formation of the distinctive Mg–Zn–Cl-integrated interface.

The XRD profiles indistinctly illustrated the structural differences between $ZnCl_2$- and $Zn(TfO)_2$-modified Mg. In this study, grazing incidence XRD (GI-XRD) was employed to predominantly analyze surface characteristics. The diffraction patterns of the modified electrodes showed distinct peaks corresponding to the hexagonal close-packed (hcp) structure of Zn, in addition to the hcp structure of Mg substrate, irrespective of pretreatment solutions (Fig. 7). Notably, the shapes of these diffraction peaks showed variations; Mg electrodes modified with $ZnCl_2$ exhibited smaller and broader hcp Zn peaks than those modified with $Zn(TfO)_2$, suggesting a more amorphous Zn on the $ZnCl_2$-modified Mg electrodes. Moreover, the GI-XRD profiles provided evidence for the Mg–Zn alloy formation in the $ZnCl_2$-modified Mg electrodes [57]. These findings aligned well with the above STEM results.

Overall, these observations suggested that $ZnCl_2$-modification imparted excellent electrochemical Mg deposition–dissolution performance, while the effect of $Zn(TfO)_2$-modification was negligible. Therefore, the formation of a specific Mg–Zn–Cl-integrated interface from $ZnCl_2$ was crucial for achieving optimal interfacial and electrochemical characteristics.

As shown in the EDX and corresponding EBSD profiles, the interfacial Mg–Zn–Cl-integrated compounds play an impressive role as an artificial solid–electrolyte interface because Mg dissolution and subsequent deposition occur beneath the interface (Fig. 8). The crystallite size and orientation of the deposited Mg beneath the interface substantially differ from those of the substrate. The bulk substrate Mg comprises relatively coarse grains with the (0001) plane orientation owing to the metallurgical feature of the extruded Mg [7]. As described earlier, the undesired cell failure is induced by the intrusion of Mg deposits into the micropores of separators and subsequent percolation of the deposited Mg between the working and counter electrodes [11]. For the $ZnCl_2$-modified Mg, the initially prepared interface with a whisker morphology becomes a compact layer upon compression with a spring during cell assembly, likely enhancing the uniformity of coverage owing to the flexible nature of the amorphous interface (Fig. S17). Mg deposition and dissolution take place through the artificial interface; thus, the intrusion of Mg deposits is physically suppressed. This interfacial behavior is responsible for the remarkably enhanced cycle performances of the cells with $ZnCl_2$-modified Mg electrodes (Figs. 2 and 3).

The stability of the $ZnCl_2$-based artificial interface was further assessed using the results of XRD, SEM, and ICP-MS measurements. As shown in Fig. 7b, the relative peak intensities of hcp Mg increased for the $Zn(TfO)_2$-modified Mg electrodes after a single Mg dissolution, suggesting that the Mg substrate was exposed to the surface, possibly accompanied with the degradation of the Zn layer derived from $Zn(TfO)_2$. The cross-sectional SEM images of the step-by-step morphological evolution of the $Zn(TfO)_2$-modified Mg electrodes represent the detachment of the Zn-based interface from the surface after a single dissolution process (Fig. S18). In contrast, because of less change in the relative peak intensities of hcp Mg, the surface was covered with amorphous Zn, and the exposure of the Mg substrate to the surface was suppressed even after one Mg dissolution process for the $ZnCl_2$-modified Mg electrodes (Fig. 7a). The observations of the corresponding step-by-step morphological evolution also support better stability and adhesivity of the Mg–Zn–Cl-integrated compounds as they remain on the surface even after the dissolution and deposition processes (Fig. S19). The superior stability of the interface derived from $ZnCl_2$ was also evidenced by the ICP-MS measurements of the electrolytes obtained from the cycled cells. The concentration of $Zn^{2+}$ in the cycled electrolytes using the $ZnCl_2$-modified Mg electrodes was the same as that obtained from the cells with the unmodified Mg electrodes, whereas approximately 300 times the amount of $Zn^{2+}$ was detected from the electrolytes cycled with the $Zn(TfO)_2$-modified Mg electrodes (Table 1). The strong binding of $Zn^{2+}$ by the remaining $Cl^-$ and the resulting less solubility of the artificial interface may be responsible for the remarkable physical and chemical stabilities of the Mg–Zn–Cl-integrated interface.

## 4. Conclusion

The screening of organic and inorganic separators provides significant insights into the failure of cells with Mg negative electrodes, caused by the undesired intrusion of deposits into the microporous separator and consequent clogging and/or percolation. Apart from the unreasonable thick separator utilization, a functional interface, which can prevent such a serious scenario, was constructed upon simple galvanic replacement reactions of Mg electrodes with less reductive metal species. Among the various metal and anionic species used for surface modification, a certain $ZnCl_2$-based solution was found to impart a particularly favorable artificial interface for Mg deposition and dissolution. The $ZnCl_2$-modified interface represents remarkably stable galvanostatic cycling over 1500 and 750 h at an areal capacity of 1 and 5 mAh $cm^{-2}$ at the same applied current density of 1 mA $cm^{-2}$ with an exceptionally small overpotential using halide-free WCA-based electrolytes. By taking the utilization ratio of Mg electrodes into account, the present combination can serve as the optimal Mg-electrolyte interface with outstanding electrochemical performance using sufficiently thin Mg electrodes ($t = 40$ µm), whereas thick Mg electrodes (typically $t >$ 100 µm) were utilized at a limited utilization ratio (ca. 1–2 %) for galvanostatic measurements in preceding works (Fig. 9) [58]. In addition, the proposed interface enables the use of thinner and lighter organic PTFE separators compared to GF separators. The comprehensive mechanistic studies revealed the specific function of the Mg–Zn–Cl-integrated artificial interface. The electrochemical Mg deposition–dissolution takes place beneath such interface, as evidenced by EBSD analyses. The amorphous nature induced by Cl integration is beneficial in stabilizing the interface during successive changes in the morphology of Mg electrodes associated with electrochemical deposition–dissolution cycling. The crystalline Zn-based interface derived from $Zn(TfO)_2$ showed poor electrochemical cycling performance owing to the detachment of the interface from the surface upon base Mg deposition/dissolution. ICP-MS analyses on the cycled electrolytes further

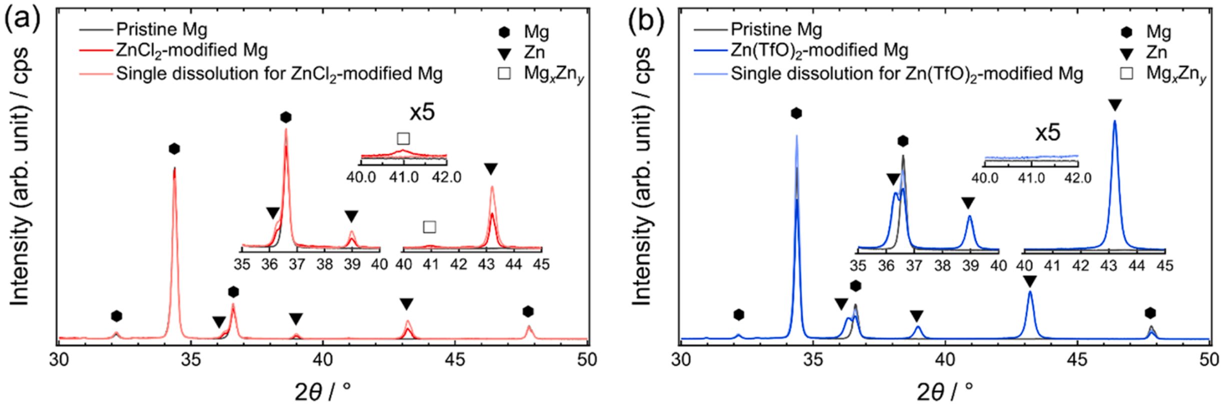

**Fig. 7.** GI-XRD profiles of pristine and (a) $ZnCl_2$- and (b) $Zn(TfO)_2$-modified Mg electrodes. The profiles of modified Mg electrodes after one dissolution are also presented.

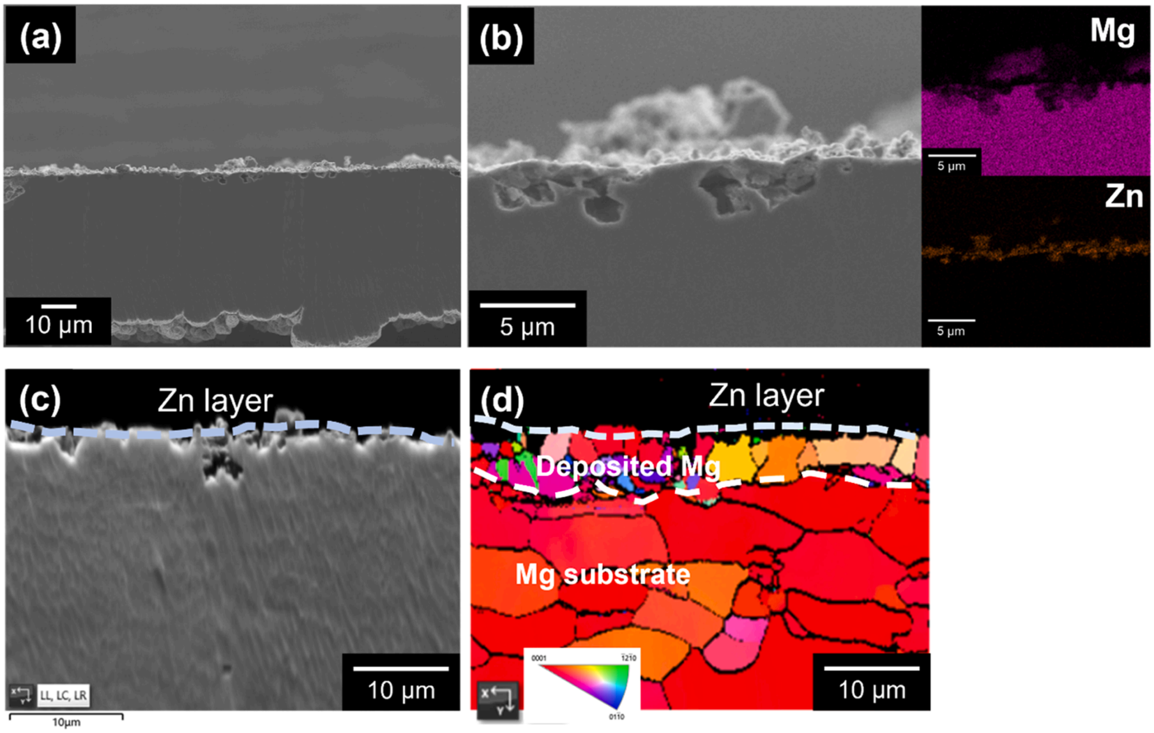

**Fig. 8.** (a) SEM, (b) SEM-EDX, and (c), (d) EBSD profiles of the cross-sectional images of the $ZnCl_2$-modified Mg after one dissolution–deposition cycle at an areal capacity of 1 mAh $cm^{-2}$.

**Table 1**
$Zn^{2+}$ concentration in the electrolytes extracted from the cycled [Mg or modified Mg || Cu] cells determined using ICP-MS measurements.

| Mg electrodes | Zn concentration / ppm |
|---|---|
| Unmodified | 0.09 |
| $ZnCl_2$-modified | 0.13 |
| $Zn(TfO)_2$-modified | 37 |

verify the superior stability of the Mg–Zn–Cl-integrated interface (Table 1).

The limitation of the separator choice to thick GF separators in Mg batteries inhibits the investigation of battery cycling properties under rather harsh, lean electrolyte, and high utilization conditions. The techniques developed in this work can pave the way for such an unexplored but extremely important research area toward RMB realization. Comprehensive studies on the amount of electrolyte dominating the electrochemical Mg deposition–dissolution behavior at different utilization ratios are under way.

## CRediT authorship contribution statement

**Toshihiko Mandai:** Conceptualization, Data curation, Formal analysis, Funding acquisition, Investigation, Project administration, Resources, Validation, Writing – original draft, Writing – review & editing. **Umi Tanaka:** Data curation, Formal analysis, Writing – review & editing. **Mariko Watanabe:** Data curation, Formal analysis.

## Declaration of competing interest

The authors declare that they have no known competing financial interests or personal relationships that could have appeared to influence the work reported in this paper.

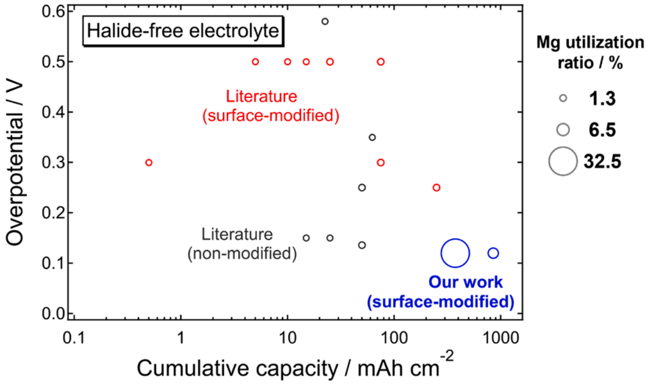

**Fig. 9.** Comparison of galvanostatic Mg deposition–dissolution performances using unmodified and surface-modified Mg electrodes in halide-free electrolytes with those of previously reported cells. The plots are based on three parameters: overpotential for deposition–dissolution (*y*-axis), cumulative capacity (*x*-axis), and Mg utilization ratio (diameter). The utilization ratio is calculated using the following equation: (utilization [%]) = 100 × {(areal capacity of each single electrochemical process [mAh $cm^{-2}$]) × 2.6 [μm $mAh^{-1}$ $cm^2$]}/$t_{Mg}$ [μm]. The details of literature data are described in Table S2.

## Data availability

Data will be made available on request.

## Acknowledgments

This work was supported by the NEXT Center of Innovation Program (Grant number JPMJPF2016) of the Japan Science and Technology Agency and the Grant-in-Aid for Scientific Research (Grant number JP21K05263) of the Japan Society for the Promotion of Science. The authors acknowledge the NIMS Battery Research Platform for their assistance with SEM, EBSD, STEM, EELS, and XPS.

## Supplementary materials

Supplementary material associated with this article can be found, in the online version, at doi:10.1016/j.ensm.2024.103302.

## References

[1] J. Zhang, Z. Chang, Z. Zhang, A. Du, S. Dong, Z. Li, G. Li, G. Cui, ACS Nano 15 (2021) 15594–15624.

[2] C.-H. Shin, H.-Y. Lee, C. Gyan-Barimah, J.-H. Yu, J.-S. Yu, Chem. Soc. Rev. 52 (2023) 2145–2192.

[3] K. Shimokawa, T. Atsumi, N.L. Okamoto, T. Kawaguchi, S. Imashuku, K. Wagatsuma, M. Nakayama, K. Kanamura, T. Ichitsubo, Adv. Mater. 33 (2021) 2007539.

[4] Y. Xiu, A. Mauri, S. Dinda, Y. Pramudya, Z. Ding, T. Diemant, A. Sarkar, L. Wang, Z. Li, W. Wenzel, M. Fichtner, Z. Zhao-Karger, Angew. Chem. Int. Ed. 62 (2023) e202212339.

[5] T. Mandai, H. Somekawa, Chem. Commun. 56 (2020) 12122–12125.

[6] T. Mandai, H. Somekawa, Batter. Supercaps 5 (2022) e202200153.

[7] A. Maddegalla, A. Mukherjee, J.A. Blázquez, E. Azaceta, O. Leonet, A.R. Mainar, A. Kovalevsky, D. Sharon, J.-F. Martin, D. Sotta, Y. Ein-Eli, D. Aurbach, M. Noked, ChemSusChem 14 (2021) 4690–4696.

[8] J.T. Herb, C.A. Nist-Lund, Craig, B. Arnold, ACS Energy Lett 1 (2016) 1227–1232.

[9] W. Zhao, Z. Pan, Y. Zhang, Y. Liu, H. Dou, Y. Shi, Z. Zuo, B. Zhang, J. Chen, X. Zhao, X. Yang, Angew. Chem. Int. Ed. 61 (2022) e202205187.

[10] T. Mandai, M. Yao, K. Sodeyama, A. Kagatsume, Y. Tateyama, H. Imai, J. Phys. Chem. C 127 (2023) 10419–10433.

[11] T. Mandai, ACS Appl. Mater. Interfaces 12 (2020) 39135–39144.

[12] J. Eaves-Rathert, K. Moyer, M. Zohair, C.L. Pint, Joule, 4 (2020) 1324–1336.

[13] X. Liu, A. Du, Z. Guo, C. Wang, X. Zhou, J. Zhao, F. Sun, S. Dong, G. Cui, Adv. Mater. 34 (2022) 2201886.

[14] Z. Ma, M. Kar, C. Xiao, M. Forsyth, D.R. MacFarlane, Electrochem. Commun. 78 (2017) 29–32.

[15] Y. Yu, A. Baskin, C. Valero-Vidal, N.T. Hahn, Q. Liu, K.R. Zavadil, B.W. Eichhorn, D. Prendergast, E.J. Crumlin, Chem. Mater. 29 (2017) 8504–8512.

[16] J. Luo, S. He, T. Leo Liu, ACS Energy Lett. 2 (2017) 1197–1202.

[17] T. Mandai, M. Watanabe, J. Mater. Chem. A 11 (2023) 9755–9761.

[18] S.-B. Son, T. Gao, S.P. Harvey, K. Xerxes Steirer, A. Stokes, A. Norman, C. Wang, A. Cresce, K. Xu, C. Ban, Nat. Chem. 10 (2018) 532–539.

[19] Y. Sun, Q. Zou, W. Wang, Y.-C. Lu, ACS Energy Lett. 6 (2021) 3607–3613.

[20] J.H. Kwak, Y. Jeoun, S.H. Oh, S. Yu, J.-H. Lim, Y.-E. Sung, S.-H. Yu, H.-D. Lim, ACS Energy Lett. 7 (2022) 162–170.

[21] X. Li, T. Gao, F. Han, Z. Ma, X. Fan, S. Hou, N. Eidson, W. Li, C. Wang, Adv. Energy Mater. 8 (2018) 1701728.

[22] Y. Zhao, A. Du, S. Dong, F. Jiang, Z. Guo, X. Ge, X. Qu, X. Zhou, G. Cui, ACS Energy Lett. 6 (2021) 2594–2601.

[23] H. Park, H.-K. Lim, S.H. Oh, J. Park, H.-D. Lim, K. Kang, ACS Energy Lett. 5 (2020) 3733–3740.

[24] J. Bae, H. Park, X. Guo, X. Zhang, J.H. Warner, G. Yu, Energy Environ. Sci. 14 (2021) 4391–4399.

[25] C. Pechberty, A. Hagopian, J.-B. Ledeuil, D. Foix, J. Allouche, J.-N. Chotard, O. Lužanin, J. Bitenc, R. Dominko, R. Dedryvére, J.-S. Filhol, L. Stievano, R. Berthelot, J. Mater. Chem. A 10 (2022) 12104–12113.

[26] K. Tang, A. Du, S. Dong, Z. Cui, X. Liu, C. Lu, J. Zhao, X. Zhou, G. Cui, Adv. Mater. 32 (2020) 1904987.

[27] Z. Meng, Z. Li, L. Wang, T. Diemant, D. Bosubabu, Y. Tang, R. Berthelot, Z. Zhao-Karger, M. Fichtner, ACS Appl. Mater. Interfaces 13 (2021) 37044–37051.

[28] J. Zhang, X. Guan, R. Lv, D. Wang, P. Liu, J. Luo, Energy Storage Mater. 26 (2020) 408–413.

[29] G. Yang, Y. Li, C. Zhang, J. Wang, Y. Bai, C.Y.J. Lim, M.-F. Ng, Z. Chang, S. Kumar, Z. Sofer, W. Liu, Z.W. She, Nano Lett. 22 (2022) 9138–9146.

[30] D. Chinnadurai, W.Y. Lieu, S. Kumar, G. Yang, Y. Li, Z.W. She, Nano Lett. 23 (2023) 1564–1572.

[31] T. Shen, C. Luo, Y. Hao, Y. Chen, Front. Chem. 8 (2020) 459.

[32] D. Aurbach, H. Gizbar, A. Schechter, O. Chusid, H.E. Gottlieb, Y. Gofer, I. Goldberg, J. Electrochem. Soc. 149 (2002) A115–A121.

[33] K. Tang, A. Du, X. Du, S. Dong, C. Lu, Z. Cui, L. Li, G. Ding, F. Chen, X. Zhou, G. Cui, Small 16 (2020) 2005424.

[34] J. Muldoon, C.B. Bucur, A.G. Oliver, J. Zajicek, G.D. Allred, W.C. Boggess, Energy Environ. Sci. 6 (2013) 482–487.

[35] S. Jiao, J. Zheng, Q. Li, X. Li, M.H. Engelhard, R. Cao, J.-G. Zhang, W. Xu, Joule 2 (2017) 110–124.

[36] R. Pathak, K. Chen, A. Gurung, K.M. Reza, B. Bahrami, J. Pokharel, A. Baniya, W. He, F. Wu, Y. Zhou, K. Xu, Q. Qiao, Nat. Commun. 11 (2020) 93.

[37] N. Zhu, X. Mao, G. Wang, M. Zhu, H. Wang, G. Xu, M. Wu, H.K. Liu, S.-X. Dou, C. Wu, J. Mater. Chem. A 9 (2021) 13200–13208.

[38] M. Ue, K. Sakaushi, K. Uosaki, Mater. Horiz. 7 (2020) 1937–1954.

[39] Z. Zhang, Z. Cui, L. Qiao, J. Guan, H. Xu, X. Wang, P. Hu, H. Du, S. Li, X. Zhou, S. Dong, Z. Liu, G. Cui, L. Chen, Adv. Energy Mater. (2017) 1602055.

[40] Z. Zhao-Karger, M.E.G. Bardaji, O. Fuhr, M. Fichtner, J. Mater. Chem. A 5 (2017) 10815–10820.

[41] T. Mandai, Y. Youn, Y. Tateyama, Mater. Adv. 2 (2021) 6283–6296.

[42] T. Pavčnik, M. Lozinšek, K. Pirnat, A. Vizintin, T. Mandai, D. Aurbach, R. Dominko, J. Bitenc, ACS Appl. Mater. Interfaces 14 (2022) 26766–26774.

[43] T. Mandai, H. Naya, H. Masu, J. Phys. Chem. C 127 (2023) 7987–7997.

[44] T. Mandai, Y. Akita, S. Yagi, M. Egashira, H. Munakata, K. Kanamura, J. Mater. Chem. A 5 (2017) 3152–3156.

[45] R. Davidson, A. Verma, D. Santos, F. Hao, C. Fincher, S. Xiang, J. Van Buskirk, K. Xie, M. Pharr, P.P. Mukherjee, S. Banerjee, ACS Energy Lett. 4 (2019) 375–376.

[46] R. Davidson, A. Verma, D. Santos, F. Hao, C.D. Fincher, D. Zhao, V. Attari, P. Schofield, J. Van Buskirk, A. Fraticelli-Cartagena, T.E.G. Alivio, R. Arroyave, K. Xie, M. Pharr, P.P. Mukherjee, S. Banerjee, Mater. Horiz. 7 (2020) 843–854.

[47] R. Lv, X. Guan, J. Zhang, Y. Xia, J. Luo, Nat. Sci. Rev. 7 (2020) 333–341.

[48] T. Yim, S.-G. Woo, S.-H. Lim, J.-Y. Yoo, W. Cho, M.-S. Park, Y.-K. Han, Y.-J. Kim, J. Yu, ACS Sustain. Chem. Eng. 5 (2017) 5733–5739.

[49] S.-J. Kang, S.-C. Lim, H. Kim, J.W. Heo, S. Hwang, M. Jang, D. Yang, S.-T. Hong, H. Lee, Chem. Mater. 29 (2017) 3174–3180.

[50] L.K. Chellappan, J. Kvello, J.R. Tolchard, P.I. Dahl, S.M. Hanetho, R. Berthelot, A. Fiksdahl, K. Jayasayee, ACS Appl. Energy Mater. 3 (2020) 9585–9593.

[51] W. Ren, D. Wu, Y. NuLi, D. Zhang, Y. Yang, Y. Wang, J. Yang, J. Wang, ACS Energy Lett. 6 (2021) 3132–3220.

[52] I.U. Mohsin, S. Riedel, Y. Xiu, Z. Z.-Karger, C. Ziebert, Batter. Supercaps (2023) e202300137.

[53] N. Jiang, D. Su, J.C.H. Spence, Ultramicroscopy 109 (2008) 122–128.

[54] K. Giannakopoulos, N. Boukos, A. Travlos, J. Phys. Conf. Ser. 10 (2005) 121–124.

[55] C. Liao, N. Sa, B. Key, A.K. Burrell, L. Cheng, L.A. Curtiss, J.T. Vaughey, J.-J. Woo, L. Hu, B. Pan, Z. Zhang, J. Mater. Chem. A 3 (2015) 6082–6087.

[56] Y. Yang, W. Wang, Y. Nuli, J. Yang, J. Wang, ACS Appl. Mater. Interfaces 11 (2019) 9062–9072.

[57] K. Yan, J. Bai, H. Liu, Z.-Y. Jin, J. Magnes. Alloy 5 (2017) 336–339.

[58] T. Wen, Y. Deng, B. Qu, G. Huang, J. Song, C. Xu, A. Du, Q. Xie, J. Wang, G. Cui, D.-L. Peng, X. Zhou, F. Pan, ACS Energy Lett. 8 (2023) 4848–4861.